RSC Advances

ROYAL SOCIETY OF CHEMISTRY

www.rsc.org/advances

Electrochemical Deposition of Manganese Oxide-Phosphate-Reduced Graphene Oxide Composite and Electrocatalysis of Oxygen Evolution Reaction

Ahamed Irshad and Nookala Munichandraiah*

Department of Inorganic and Physical Chemistry
Indian Institute of Science, Bangalore - 560012, India.

ABSTRACT

A composite of manganese oxide and reduced graphene oxide (rGO) is prepared in a single step electrochemical reduction process in a phosphate buffer solution for studying as an electrocatalyst for oxygen evolution reaction (OER). The novel composite catalyst, namely, MnOx-Pi-rGO, is electrodeposited from a suspension of graphene oxide (GO) in a neutral phosphate buffer solution consisting of $KMnO_4$. The manganese oxide incorporates phosphate ions and deposits on rGO sheet, which in turn is formed on the substrate electrode by electrochemical reduction of GO in the suspension. The OER is studied at MnOx-Pi-rGO catalyst in a neutral phosphate electrolyte by linear sweep voltammetry. The results indicate a positive influence of rGO in the catalyst. By varying the ratio of $KMnO_4$ and GO in the deposition medium and performing linear sweep voltammetry for OER, the optimum composition of the deposition medium is obtained as 20 mM $KMnO_4$ + 6.5 % GO in 0.1 M phosphate buffer solution of pH 7. Under identical conditions, the MnOx-Pi-rGO catalyst exhibits 6.2 mA cm^{-2} OER current against 2.9 $mAcm^{-2}$ by MnOx-Pi catalyst at 2.05 V in neutral phosphate solution. The Tafel slopes measured for OER at MnOx-Pi and MnOx-Pi-rGO are similar in magnitude at about 0.180 V $decade^{-1}$. The high Tafel slopes are attributed to partial dissolution of the catalyst during oxygen evolution. The O_2 evolved at the catalyst is measured by water displacement method and the positive role of rGO on catalytic activity of MnOx-Pi is demonstrated.

Keywords: MnOx-Pi catalyst, rGO, electrochemical deposition, water oxidation reaction.

*Corresponding author; e-mail: muni@ipc.iisc.ernet.in; Tel: +91-80-2293 3183

1. INTRODUCTION

Water splitting is one of the promising routes for storage of energy storage in the form of hydrogen. The process involves reduction of H^+ ions to produce H_2 at the cathode and oxidation of OH^- ions to O_2 at the anode. In these reactions, oxygen evolution reaction (OER) is sluggish in kinetics and requires an active and stable electrocatalyst.[1] Most commonly used catalysts in acidic media involve compounds of iridium [2,3] or ruthenium [3,4], which are rare, expensive and unstable. On the other hand, oxides or hydroxides of many non-precious elements, such as iron, [5,6] cobalt [7,8] and nickel [9,10] have been explored as oxygen evolution catalysts (OECs) in alkaline media. Manganese is a preferred choice owing to its low price, high abundance, low toxicity and possibility to design functional models of the biological catalyst.

Several manganese oxides such as MnO_2,[11,12] Mn_2O_3,[13,14] Mn_3O_4[15,16] and $MnFe_2O_4$[17,18] exhibit catalytic activity towards OER in alkaline solutions. Ohsaka and co-workers reported that electrochemically deposited MnOx nanorods exhibited high performance in basic solutions and the activity decreased in acidic and neutral media.[19] In another study, Tamura et al., demonstrated that overpotential of 300 mV at a current density of 1 mA cm^{-2} at pH 14 increased considerably to 610 mV at pH 7 on MnO_2.[20] Several other manganese compounds including MnOOH [21] and MnO_2-Mn_2O_3 composite,[22] also require overpotentials in the range 500-700 mV in neutral electrolytes. According to a report by Takashima et al.,[23] Mn^{3+} species in the catalyst play a key role in water oxidation, and the decreased activity under neutral or acidic condition is due to the instability of Mn^{3+}. At higher pH, Mn^{3+} is stable whereas Mn^{3+} ions disproportionate to produce Mn^{2+} and Mn^{4+} ions at pH < 9. Recently, amorphous manganese oxides (MnOx) were deposited by anodic oxidation of Mn^{2+} ions in phosphate (MnOx-Pi) and acetate (MnOx-Ac) buffer solutions and used as electrocatalysts for OER. [24,25]

Electronic conductivity of Mn compounds is generally low. The electronic conductivity can be improved by interfacing the catalyst with a highly conductive material such as graphene,[26,27] carbon nanotubes [28,29] or activated carbons.[30] Recently, graphene has emerged as an attractive support for catalysts because of its high surface area, excellent charge transport, good mechanical properties and superior chemical as well as electrochemical stability.[31,32] In the present work, a composite of MnOx and reduced graphene oxide (rGO) is prepared by electrochemical deposition in a single step in a neutral phosphate solution. An analysis of the electrodeposited material suggests the presence of phosphorous in a large quantity. High catalytic activity of Co oxide prepared in phosphate solution is reported in the literature and it is referred to as Co-Pi.[33,34] Similar to these reports, the MnOx prepared in phosphate solution in the present study is referred to as MnOx-Pi. Generally electrooxidation of Mn^{2+} ions to deposit MnOx is well known.[35,36] Instead, electrochemical reduction of MnO_4^- ions is adopted in the present study for the purpose of codepositing MnOx and rGO. Electrochemical reduction of graphene oxide (GO) to form rGO on substrate electrode is also reported in the literature.[37,38] Thus, the simultaneous electrochemical reduction of MnO_4^- ions and GO in phosphate buffer solution produces MnOx-Pi-rGO, which exhibits a high catalytic activity towards OER in neutral phosphate buffer solution. Results of the experiments conducted under identical conditions using MnOx-Pi and MnOx-Pi-rGO suggest that rGO imparts a substantial improvement on the catalytic activity of MnOx-Pi towards OER.

2. EXPERIMENTAL SECTION

2.1. Reagents, Materials and Characterizations

Analytical grade KH_2PO_4, K_2HPO_4 and $KMnO_4$ (all from Merck) were used as received. All solutions were prepared using double distilled water. Phosphate buffer solution was prepared

by mixing calculated volumes of 0.1 M KH_2PO_4 and 0.1 M K_2HPO_4 solutions. The solution pH was maintained at 7.0, unless otherwise stated. The physical characterization studies of the materials were carried out by using scanning electron microscopy (SEM), transmission electron microscopy (TEM), energy dispersive X-ray analysis (EDXA), X-ray photoelectron spectroscopy (XPS) and Raman spectroscopy. For SEM images, Ultra 55 scanning electron microscope equipped with EDXA system at 20 kV was used. TEM images were recorded using FEI Tecnai T-20 200 kV transmission electron microscope. Surface compositions of the electrodeposits were analyzed by XPS using SPECS GmbH spectrometer (Phoibos 100 MCD Energy Analyzer) with Mg K_α radiation. Raman spectra were collected using LabRam HR (UV) system at an excitation wavelength of 532 nm. Sheet resistance was measured by four-probe Van der Pauw method using Agilent Device Analyzer B1500A. Electrochemical deposition and OER studies were conducted using PARC EG&G potentiostat/galvanostat model Versastat II. A Pt foil substrate (area: 0.5 cm^2) for the working electrode, two large Pt foil auxiliary electrodes and a saturated calomel reference electrode (SCE) in a glass cell were used. Oxygen produced during electrolysis was detected by monitoring its reduction on a Pt-rotating disc electrode (d - 3 mm) in an air-tight glass cell. Oxygen gas was quantitatively measured in a burette by water displacement method using a large area (5 cm^2) electrode. Mass variation during electrochemical depositions was monitored by using CH Instruments potentiostat/galvanostat model 400A with an electrochemical quartz crystal microbalance (EQCM). For these experiments, a small Teflon cell with Pt-coated quartz crystal (8 M Hz, area - 0.205 cm^2, sensitivity - 0.146 Hz ng^{-1} cm^2) as the working electrode, Pt wire counter electrode and Ag/AgCl, Cl^- (3M) reference electrode was used. Electrochemical impedance spectroscopy (EIS) measurements were performed at 10 mV ac excitation signal over the frequency range of

100 kHz - 0.10 Hz. Current density values are reported on the basis of geometrical area of the electrode. All potential values are converted to reversible hydrogen electrode (RHE) scale using the equation, $E_{RHE} = E_{SCE} + E^0_{SCE} + 0.059*pH$, where E_{SCE} is the measured potential using SCE reference and E^0_{SCE} is the standard potential of SCE at 25 ºC (0.242 V), unless otherwise stated.

2.2. Preparation of graphene oxide dispersion

Graphite powder was converted into graphite oxide (GtO) by a modified Hummers and Offemann method.[39] In a typical synthesis, 3.0 g graphite powder was added to 69 ml conc. H_2SO_4 containing 1.5 g $NaNO_3$. The mixture was stirred for 1 h at ambient temperature. The container was cooled in an ice-bath, and 9.0 g $KMnO_4$ was added slowly under stirring. The container was removed from the ice-bath and allowed to reach the room temperature. Double-distilled water was added slowly in two aliquots of 138 ml and 420 ml in about 15 min intervals. Then, 7.5 ml of 30 % H_2O_2 was added and the color of the suspension changed from yellow to brown, indicating the oxidation of graphite to graphite oxide (GtO). The product was separated by centrifugation, washed with warm water and ethanol several times, and dried at 50 ºC. About 300 mg of GtO was added to 300 ml double-distilled water and sonicated for 3 h using Misonix ultra sonicator model S4000-010. The dispersion was allowed to settle for 24 h. The supernatant solution was collected for further use as graphene oxide (GO) dispersion and the settled residue was discarded. GO concentration of 0.7 mg ml^{-1} was obtained by this scheme.

2.3. Preparation of MnOx-Pi-rGO Catalyst

MnOx-Pi was deposited on a Pt foil electrode at -1.05 V vs. SCE for 30 min from 0.1 M phosphate solution (pH 7.0) containing 20 mM $KMnO_4$ under stirring condition. For studying the effect of rGO towards OER activity, MnOx-Pi-rGO was also deposited under

identical condition, except that the deposition bath contained GO additionally in it. The electrodes were washed well with double distilled water and air dried. OER activity of the deposit was measured by subjecting to linear sweep voltammetry at 5 mV s^{-1} in phosphate buffer (pH 7.0) solution.

3. RESULTS AND DISCUSSIONS

3.1. Simultaneous electrochemical deposition

Electrochemical deposition of MnOx-Pi catalyst was performed on a Pt foil electrode from 0.1 M phosphate buffer (pH 7.0) solution containing 20 mM $KMnO_4$ at -1.05 V vs. SCE (Fig. 1(i)). In neutral aqueous condition, reduction of MnO_4^- proceeds via the following reaction,[40]

$$MnO_4^- + 2\ H_2O + 3\ e^- \rightarrow MnO_2 + 4\ OH^- \quad (1)$$

Since the electrolyte has a large amount of phosphate ions, incorporation of phosphate leading to the formation of a manganese-oxide-phosphate catalyst (MnOx-Pi) is expected. The process is similar to the deposition of MnOx-Pi by the oxidation of Mn^{2+} ions in phosphate solution,[24] but for the reduction of Mn^{7+} ions in the present study. It is reported that Mn^{3+} is stabilized by the phosphate group in the catalyst structure.[41] As described below in the section of XPS, the majority of Mn is present in 3+ oxidation state due to the presence of phosphate in the deposit. Furthermore, phosphate in the catalyst is known to play a crucial role in the proton coupled electron transfer (PCET) mediated mechanism of OER and stability of the catalyst.[42,43] Recent studies on the structure and activity of a Mn-phosphate catalyst suggested the role of phosphates as bridging ligands interconnecting two or more manganese ions.[44] The amperogram recorded during the deposition of MnOx-Pi (Fig. 1(i)) exhibits three distinct regions: (i) a sudden rise in the current followed by a rapid decay, (ii) a rise and fall in the current to form a peak and

(iii) a steady decrease in the current to reach a limiting current. This indicates that MnOx-Pi deposition is not a simple diffusion-controlled process but, proceeds via a nucleation-growth pathway as reported in the case of anodically deposited MnOx-Pi catalyst.[45] The initial rise and fall in the current to form a peak in the amperogram is due to primary nucleation on the electrode surface. The current peak is the result of depletion of MnO_4^- ions in the vicinity of the electrode. As the depletion zone expands, current falls as function of a $t^{-1/2}$, which is the characteristics of a diffusion-controlled growth of the deposited material. However, the current does not decay to zero, due to the parasitic hydrogen evolution reaction. Application of higher negative voltage causes vigorous H_2 evolution and consequently, hinders the electrodeposition of MnOx-Pi. Electrochemical reduction of GO to rGO was reported as a convenient and fast route to synthesize high quality graphene nanosheets in a large scale.[37,38] The applied negative potentials facilitate reduction of oxygen functionalities (-OH, C-O-C on the planes and –COOH on the edges) of GO adsorbed on substrate electrode resulting in the deposition of rGO sheets.[37] Cyclic voltammograms of a glassy carbon electrode recorded in a suspension of GO exhibited a reduction current peak at -1.20 V vs. SCE which is attributed to the reduction of GO to rGO.[37] Fig. 1(ii) shows the current-time curve for the GO reduction at -1.05 V vs. SCE in 0.1 M phosphate buffer solution (pH 7.0) containing GO of concentration 0.2 mg ml^{-1} as suspension. A gradual decrease in the current density from 7.0 mA cm^{-2} to a steady state value of 2.9 mA cm^{-2} is observed. A black coating on the electrode surface was visually observed, indicating the reduction of GO, and concomitant deposition of rGO on the substrate. Since, both MnOx-Pi and rGO are deposited at -1.05 V vs. SCE from phosphate solutions containing $KMnO_4$ and GO, respectively, simultaneous deposition and formation of hybrid MnOx-Pi-rGO from a mixed $KMnO_4$-GO solution in the phosphate buffer is expected. Fig. 1(iii) shows the

variation in the current as the function of time during the deposition of MnOx-Pi-rGO from 0.1 M phosphate solution (pH 7.0) containing 20 mM $KMnO_4$ and GO (amount of GO was adjusted to 6.5 % with respect to the weight of $KMnO_4$). The current-time trace in Fig. 1(iii) shows the nucleation-growth features as observed in the case of deposition of MnOx-Pi (Fig. 1(i)), but with a higher magnitude of the current. The increased value of current indicates that the reaction involves not only MnOx-Pi deposition but GO reduction also. Thus, these experiments indicate that the MnOx-Pi-rGO hybrid material can be obtained by the simultaneous electrochemical reduction of MnO_4^- and GO in neutral phosphate buffer solution.

MnO_2 is generally prepared by electrochemical oxidation of Mn^{2+} ions in the electrolyte,[35,36] similar to the procedures used for electrodeposition of MnOx-based catalysts for OER.[24,25] However, the catalyst in the present study is prepared by reducing Mn^{7+} ions. This method is adopted for facilitating compatibility for the preparation of rGO. It is reported [37,38] that an aqueous suspension of graphene oxide can be reduced electrochemically to produce rGO deposit on electrodes. Therefore, graphene oxide suspension in $KMnO_4$ solution is used to reduce simultaneously Mn^{7+} ions and graphene oxide. The electrodeposition of MnOx-Pi-rGO composite is achieved successfully, for the first time in the literature.

3.2. EQCM study

It was intended to monitor the electrodeposition process in-situ by EQCM. This technique allows us to quantitatively measure the mass of the deposit on the electrode surface as a function of time. It is seen from Fig. 2(i) that the cathodic polarization of Pt coated quartz crystal electrode to -1.05 V vs. SCE in MnO_4^- solution causes an increase in the mass of the electrode. The mass increases rapidly to 4.5 µg cm^{-2} within first 10 s and thereafter increases gradually to 10.8 µg cm^{-2} at 60 s. This also suggests an initial rapid nucleation followed by a

gradual growth of the catalyst. Similar experiments were carried out for the deposition of MnOx-Pi-rGO and corresponding massogram is shown in Fig. 2(ii). In this case, mass increases to 5.3 μg cm^{-2} in the first 10 s and attains 14.5 μg cm^{-2} after 60 s. Thus, the net mass gain after 60 s of polarization at -1.05 V vs. SCE in the presence of rGO deposition is 14.5 μg cm^{-2} (Fig. 2(ii)) whereas that in the absence of rGO is 10.8 μg cm^{-2} (Fig. 2(i)). Assuming similar kinetics of deposition for MnOx-Pi in the presence and absence of GO in the deposition bath, mass of rGO in the MnOx-Pi-rGO is calculated as 3.7 μg cm^{-2}, which is about 25.5 % of the total mass.

3.3. Morphology

Morphology of the electrodeposit was studied by using SEM and TEM. As shown in Fig. 3(a), electrochemically deposited rGO sheets exhibit typical wrinkled structure with foldings. These geometric wrinkling and rippling are the result of nanoscale interlocking of rGO sheets. Corrugation and folding are inherent features of graphene, because the 2D membrane structure is thermodynamically stable via bending. These features of rGO provide enhanced mechanical properties, reduced surface energy, increased surface roughness and high density of electrochemically active sites.[46] It is also reported that corrugations in graphene sheets make electron transfer 10 times faster than at the basal plane of graphite.[47] Morphology of the electrodeposited MnOx-Pi is shown in Fig. 3(b). Several particles of 100 - 200 nm size are coalesced to form catalytic islands. Hence, it is proposed that MnOx-Pi deposits as small nuclei in the initial stages of electrolysis and then grows slowly to bigger particles. These bigger particles finally merge together to form catalytic islands. Fig. 3(c) shows the image of MnOx-Pi-rGO. The deposit preserves the nanosheet features of rGO together with MnOx-Pi catalyst particles embedded in it. It is to be noted that rGO and MnOx-Pi are not deposited in

separate zones, but both are mixed, resulting in a strong interaction between them at the molecular level. This is achieved due to the simultaneous deposition of MnOx-Pi and rGO by the present method. It is seen from TEM image (Fig. 3(d)) that the electrodeposited rGO nanosheets are folded and overlapped. The deposition of rGO in the presence of MnO_4^- leads to the formation of hybrid MnOx-Pi-rGO composite (Fig. 3(e) and (f)). The rGO sheets are decorated with nanoparticles as well as large particles of MnOx-Pi. The high resolution image for MnOx-Pi-rGO (Fig. 3(f)) shows the lattice fringes of rGO. Poor crystalline feature obtained in the SAED pattern (inset in Fig. 3(f)) suggests the amorphous nature of the MnOx-Pi deposit on the surface of rGO sheets.

3.4. Composition

The elemental composition of MnOx-Pi-rGO was determined from the EDXA spectra. The spectrum in Fig. 4a shows Mn, P, C, O and K as the major elements. Mn:P ratio varies from 2:1 to 1.5:1, indicating significant incorporation of phosphate in the catalyst layer. Also, Mn:K ratio is found to be about 3:1. Although the role of K is not clear, it is likely that K^+ ions are adsorbed on the surface of the catalyst. The presence of C peak indicates the deposition of rGO along with MnOx-Pi during the electrochemical reduction of MnO_4^- ions in phosphate solution containing GO. The distribution of elements on the substrate surface is shown by X-ray maps (Fig. 4 (c)-(e)). Elements are distributed uniformly without agglomeration. It is anticipated that the defects in the rGO sheets may act as the nucleation site for the deposition of MnOx-Pi and thus preventing agglomeration.

The chemical composition of the MnOx-Pi-rGO was also analyzed by XPS and the results are shown in Fig. 5. The survey spectrum (Fig. 5(a)) identifies Mn, P, O, K and C as the major elements present. This is in agreement with EDXA results. The Mn 2p high resolution

spectrum (Fig. 5(b)) is divided into Mn $2p_{1/2}$ at 653.6 eV and Mn $2p_{3/2}$ at 641.8 eV.[48] These peaks are further de-convoluted into two peaks. In the Mn $2p_{3/2}$ branch, the intense peak at 641.6 eV is assigned to Mn^{3+} while the smaller peak at 643.8 eV is due to Mn^{4+}.[48] The Mn^{3+}/ Mn^{4+} ratio of about 4.5 is obtained from the ratio of areas under the peaks. This suggests that the Mn present in MnOx-Pi-rGO is largely in 3+ oxidation state, which is reported to play a key role in water oxidation.[23] The peak at 132.8 eV in the P 2p spectrum (Fig. 5(c)) is consistent with phosphate. This is comparable to the binding energy of the P 2p peak observed in the case of Co-Pi [33] and Ir-Pi [49] catalysts. The high resolution C 1s peak (Fig. 5(d)) is de-convoluted into three peaks. The main peak at 284.6 eV is due to graphitic sp^2 C atoms while the small ones at 286.3 and 287.8 eV correspond to C atoms bonded with oxygenated groups.[50] It is seen that the percentage of oxygenated carbon is less than 20 % of the total carbon, indicating a significant removal of oxygen functional groups during electrochemical reduction of graphene oxide in phosphate medium. The XPS peak in O 1s region (Fig. 5(e)) is fitted to Mn-O-Mn (529.7 eV), Mn-O-H (530.8 eV) and C-OH (532.9 eV).[50] Small amount of K is also detected in XPS survey spectrum similar to the EDXA data. Hence, high resolution K 2p was also recorded (Fig. 5(f)). The spectrum shows a doublet with spin-orbit splitting of 2.8 eV. The peaks at 295.7 and 292.5 eV are assigned to K $2p_{3/2}$ and $2p_{1/2}$, respectively.[49]

3.5. Raman spectroscopy

Raman spectrum of rGO (Fig. 6(i)) shows peaks at 1344 cm^{-1} and 1596 cm^{-1}, which are assigned to D and G bands, respectively. The G band corresponds to the optical E_{2g} phonons at the Brillouin zone center due to bond stretching of the sp^2 carbon pairs, whereas the D band is associated with the second-order of zone-boundary phonons, which are activated by defects.[51,52] Thus, the intensity ratio between D and G peak (I_D/I_G) is usually used as a measure

for the degree of disorder. In the present case I_D/I_G ratio for rGO is 1.4, indicating significant disorder in the rGO sheets. However, the I_D/I_G does not always correlate well with the electronic quality of rGO.[53] After electrochemical reduction, the intensity ratio was found to be increased in most of the electrochemically prepared rGO in the literature.[53] This is attributed to a decrease in the average size of sp^2 domains. Electrochemical deposition involves the formation of new graphitic domains with smaller size but in larger number.[53] Raman spectrum of MnOx-Pi-rGO (Fig. 6(ii)) shows D and G peaks of rGO at 1352 cm^{-1} and 1604 cm^{-1}. These values are slightly shifted in comparison with that of bare rGO. Interestingly, I_D/I_G ratio is reduced to 1.1. More importantly, the spectrum in Fig. 6(ii) shows a broad peak centered at 625 cm^{-1}. This can be assigned to Mn-O stretching vibrations of the MnO_6 group.[50,54] This clearly indicates the formation of MnOx-Pi along with rGO on the electrode surface during the electrochemical reduction process.

3.6. OER activity

The catalytic activity of MnOx-Pi with and without rGO was studied using linear sweep voltammetry at 5 mV s^{-1} in neutral phosphate buffer solutions. Phosphate buffer was chosen for comparing the present result with the reported values on anodically deposited MnOx-Pi.[24,25] Also, the buffer solution annuls any change in the pH by proton release during water oxidation reaction. In the case of MnOx-Pi catalyst (Fig. 7(i)), negligibly small capacitive current flows until the potential reaches 1.65 V, the onset potential of OER. Then the current increases to 2.8 mA cm^{-2} at 2.05 V due to OER. Thus, the overpotential required to reach the onset potential of OER is about 420 mV, which is considered as large. One of the reasons for such poor catalytic activity of MnO_2 towards OER is low conductivity. Hence, it is anticipated that incorporation of highly conducting matrix such as rGO can improve the overall catalytic activity. Linear sweep

voltammogram recorded for MnOx-Pi-rGO (Fig. 7(ii)) shows that the onset of OER is 1.55 V, which is 100 mV less than that on bare MnOx-Pi. Moreover, the current density at 2.05 V for MnOx-Pi-rGO is 6.2 mA cm^{-2}, which is about 2.2 times higher in comparison with that of MnOx-Pi catalyst without rGO. Thus, the hybrid MnOx-Pi-rGO is a superior to MnOx-Pi in catalytic activity in terms of both the onset potential of OER and current density at any potential in the OER region.

3.7. Optimizations of deposition conditions

It was intended to optimize the deposition parameters for MnOx-Pi-rGO in view of the maximum catalytic activity. At first, several electrodes were made by keeping the concentration of $KMnO_4$ at 13 mM in 0.1 M phosphate buffer solution, while the weight percentage of GO in the electrolyte was gradually varied. Deposition was carried out at -1.05 V vs. SCE for 30 min and OER activity of each electrode was studied by linear sweep voltammetry at 5 mV s^{-1} in neutral phosphate buffer solution. The current density obtained at 2.05 V is plotted as a function of weight percentage of GO in the electrolyte (Fig. 8(a)). It is seen that the current is 3.3 mA cm^{-2} at 0 % GO and it increases to a maximum value of 5.5 mA cm^{-2} for 6.5 % GO. The current density values of 4.4 and 4.8 mA cm^{-2} were obtained at intermediate GO concentration of 3.4 % and 4.9 %. Since the deposition of rGO increases with an increase in GO concentration, it indicates the favorable role of rGO towards OER. However, increasing GO concentration more than 6.5 % results in a decrease in the OER current. It is expected that at higher concentration of GO, coagulation of GO increases leading to its reduced concentration in the phosphate buffer solution. Therefore, there is a decrease in rGO in the catalyst resulting in reduced catalytic activity. This is supported by the EDXA analysis of MnOx-Pi-rGO deposits prepared at different GO concentrations that the carbon content in the catalyst decreases by increasing GO

concentration beyond a particular limit (ESI, Fig. S1). In another set of experiments for the optimization of concentration of $KMnO_4$, percentage of GO in the deposition bath was fixed to 6.5 %, and then the concentration of $KMnO_4$ was varied. The deposition of the catalyst and OER analysis were carried out as above. As shown in Fig. 8(b), the OER current increases with an increase in concentration of $KMnO_4$ in the electrolyte. It reaches a maximum value of 6.2 mA cm^{-2} at 2.05 V for 20 mM concentration. The increase in current with concentration of $KMnO_4$ is attributed to enhanced rate of deposition and thus a greater loading of the MnOx-Pi at higher concentration. On the other hand, material loading beyond an optimum range diminishes the catalytic performance. This is ascribed to poor conductivity of Mn-based catalysts, which is a decisive factor at higher loading level. Also, rapid nucleation and growth of the catalyst at very high concentration causes the agglomeration of particles, which in turn reduce the available electrochemically active surface area for the catalysis. Hence, a composition of 20 mM $KMnO_4$ and 6.5 % of GO is considered as the optimum for the deposition of MnOx-Pi-rGO. Although the deposition potential is another parameter which requires optimization, it is restricted to -1.05 V vs. SCE as the deposition rate is lower at higher potentials, whereas excessive hydrogen evolution occurs at lower potentials. It was then planned to deposit MnOx-Pi-rGO at -1.05 V vs. SCE from the electrolyte with optimum concentration of GO and $KMnO_4$ at different time intervals. Results are shown in Fig. 8(c). It is seen that current increases from 4.2 mA cm^{-2} for 5 min of deposition to 4.9 mA cm^{-2} and 5.6 mA cm^{-2} for 10 and 20 min, respectively. Current density reaches a maximum of 6.2 mA cm^{-2} for 30 min of deposition. Further increase in the deposition time leads to a gradual fall in the OER performance due to low electronic and ionic conductivity of the thick MnOx-Pi catalyst. These experiments (Fig. 8(a)-(c)) establish that the best MnOx-Pi-rGO catalyst is obtained by depositing at -1.05 V vs. SCE for 30 min from

20 mM $KMnO_4$ + 6.5 % GO in 0.1 M phosphate buffer (pH 7.0) solution. The highest OER performance on this catalyst is thus summarized to 6.2 mA cm^{-2} current at 2.05 V in neutral phosphate solution.

The OER activity of MnOx-Pi-rGO catalyst on Pt is compared with the performance of similar Mn based catalysts reported in the literature (ESI, S2). For instance, hydrated $Mn_3(PO_4)_2$ was recently reported as an efficient catalyst for OER.[55] This catalyst exhibited greater catalytic activity of about 0.3 $mAcm^{-2}$ of OER current at 1.5 V vs. NHE in relation to the low currents measured on MnO, Mn_2O_3, MnO_2 and Mn_3O_4 catalysts. The OER current measured on MnOx-Pi-rGO on Pt substrate at 2.0 V vs. RHE (ie., 1.52 V vs. NHE) is about 6.0 mA cm^{-2} in the present study. Similarly, the catalytic activity of MnOx-Pi-rGO is found to be superior to electrochemically deposited amorphous Mn-oxides.[25] The higher catalytic activity of composite MnOx-Pi-rGO in the present work is attributed to the presence of rGO and method of preparation of the catalyst.

3.8. Mechanism of OER

For conducting Tafel polarization experiments, MnOx-Pi and MnOx-Pi-rGO were deposited under the optimized conditions and linear sweep voltammograms were recorded at 0.05 mV s^{-1}. The phosphate buffer solution was kept under stirring by a magnetic pellet. Very low scan rate was used to maintain the steady state conditions and stirring to avoid mass transfer limitations. The corresponding Tafel plots for MnOx-Pi and MnOx-Pi-rGO are shown in Fig. 9. At any current density value, overpotential requirement is lower for MnOx-Pi-rGO compared to MnOx-Pi, indicating the superior OER activity of the former. By extrapolating these curves to zero over potential, exchange current density for OER is obtained. The exchange current density on MnOx-Pi-rGO is 1×10^{-4} mA cm^{-2} whereas it is only 3.1×10^{-5} mA cm^{-2} on MnOx-Pi.

Nevertheless, both the catalysts show Tafel slope of 170 mV decade^{-1}, signifying a similar mechanism for OER. In neutral and alkaline medium, OER can be written as,

$$4\ OH^- \rightleftharpoons 2\ H_2O + O_2 + 4\ e^- \quad (2)$$

with reversible electrode potential (E^r) of 1.23 V vs. RHE. The generally accepted mechanism for OER is as follows.[56]

$$S + OH^- \rightleftharpoons S\text{-}OH + e^- \quad (3)$$

$$S\text{-}OH + OH^- \rightleftharpoons S{=}O + H_2O + e^- \quad (4)$$

$$2\ S{=}O \rightleftharpoons S + O_2 \quad (5)$$

where S is the substrate site, which facilitates adsorption of OH. The current density (i) and potential (E) relationship of electron-transfer controlled step may be written as,

$$i = i_0\,(1-\theta)\ e^{(1-\alpha)\ n\ F\ (E - Er)\ /\ RT} \quad (6)$$

where i_0 is exchange current density, θ is surface coverage by OH, α is transfer coefficient, E^r is reversible potential and other symbols have their usual meanings. If either (3) or (4) is the rate determining step, n=1 and then the Tafel slope (dE / dlogi) is,

$$(dE / d\log i) = 2.3\ RT / \{(1-\alpha)\ F\} \quad (7)$$

$$= (0.059/\ \{1-\alpha\})\ V \text{ at } 25\ ^oC \quad (8)$$

Assuming α = 0.5, the value of Tafel slope thus expected is 118 mV. The mechanism of OER on several perovskite catalysts was reported by Bockris and Otagawa.[57] While Tafel slopes in the range of 40 - 120 mV decade^{-1} are reported for a majority of catalysts, values in the range of 175 - 235 mV decade^{-1} are measured for $LaVO_3$ and $SrVO_3$. The unusually high Tafel slope is attributed to the oxidation of V^{3+} and Cr^{3+} in the catalysts.[57] It is likely in the present case also that Mn^{3+} present in the MnOx-Pi-rGO and MnOx-Pi catalysts undergoes oxidation to Mn^{4+}, which occurs simultaneously with OER resulting in anomalous Tafel slope of 170 mV decade^{-1}.

3.9. RDE study

The O_2 evolved during water oxidation on MnOx-Pi-rGO catalyst was detected by reduction on a Pt rotating disc electrode (RDE) in an air tight glass cell. MnOx-Pi-rGO coated electrode was prepared at -1.05 V vs. SCE for 30 min from 20 mM $KMnO_4$ + 0.1 M phosphate buffer solution (pH 7.0) containg 6.5 % GO. An electrochemical cell was assembled in phosphate buffer solution with both MnOx-Pi-rGO coated Pt and a Pt RDE as working electrodes. The electrolyte was saturated with Ar and the potential of Pt RDE was swept at 10 mV s^{-1} from 0.95 to 0.15 V at 2500 rpm (Fig. 10a(i)). Negligibly small current flows, indicating the absence of dissolved O_2 in the electrolyte. Then, electrolysis was conducted at the MnOx-Pi-rGO electrode at 1.95 V. After 1 h, the electrolysis was terminated and the Pt RDE was again subjected to linear sweep voltammetry. It is seen (Fig. 10a(ii)) that the current due to ORR increases to -0.43 mA cm^{-2} at 0.10 V. This indicates that the O_2 has evolved on MnOx-Pi-rGO electrode during electrolysis and the dissolved O_2 undergoes reduction subsequently at the RDE. Electrolysis was again continued at the MnOx-Pi-rGO and the voltammogram of ORR was recorded after every 1 h of electrolysis. As observed in Fig. 10a((iii) - (v)), the ORR current increases to -0.7, -0.8 and -0.9 mA cm^{-2}, respectively, after 2, 3 and 4 h of OER. It is worth noticing that ORR current varies almost linearly with the time of electrolysis on MnOx-Pi-rGO (Fig.10b(i)), indicating a constant rate of oxygen evolution. Experiments were also repeated with bare MnOx-Pi without rGO (Fig. 10b(ii)). As evident from Fig. 10b(ii)), ORR current is smaller during the entire period of experiment compared to the results obtained in the case of MOx-Pi-rGO (Fig. 10b(i)). These experiments clearly show that the MnOx-Pi-rGO is a better catalyst for OER than MnOx-Pi. Furthermore, the quantitative oxygen gas measurement using water displacement method also confirmed higher activity of MnOx-Pi-rGO than MnOx-Pi

(ESI, S3). Both the catalysts exhibited Faradaic efficiency above 90 % (ESI, S3). The MnOx-Pi-rGO has moderate stability in the phosphate electrolyte under prolonged electrolysis (ESI, Fig. S4). There is a decrease in OER current by about 30 % in 1 h electrolysis at 1.95 V. The decrease in activity is probably due to the formation of less active Mn^{4+} oxides by the oxidation of active Mn^{3+} species at higher anodic potential.

3.10. Electrochemical impedance spectroscopy

The superior catalytic activity of MnOx-Pi-rGO over MnOx-Pi was further confirmed from electrochemical impedance spectroscopy (EIS) studies. Nyquist plots for MnOx-Pi and MnOx-Pi-rGO electrodes at 1.95 V in 0.1 M phosphate electrolytes (pH 7.0) are shown in Fig. 11(a). In both the cases, two broad semicircles are seen. Corresponding electrical equivalent circuits are provided in Fig. 11(a) inset. The capacitive elements are replaced by constant phase elements (CPEs), denoted by Q to account for the non-uniformity of the electrode surface. The electrolyte resistance is indicated by R_s. R_f and Q_f denote the resistance and CPE of the catalyst whereas R_{ct} and Q_{dl} represent the charge transfer resistance of OER and CPE corresponding to double layer capacitance, respectively. The values of parameters obtained by fitting the impedance spectra are given in Table 1. Notably, the R_{ct} value obtained for MnOx-Pi-rGO electrode is 103 Ω which is smaller than the R_{ct} value obtained for MnOx-Pi electrode (137 Ω) without rGO. Since, the electrocatalytic activity is inversely related to the charge transfer resistance, it predicts a higher OER activity for MnOx-Pi-rGO. These results are in agreement with the voltammetric studies.

Table 1: Impedance parameters

(A) MnOx-Pi-rGO catalyst

Parameters	Value	Error (%)
R_s (Ω)	2.5	4.1
Q_f - Y_o (F s^{n-1})	0.0002	3.0
Q_f - n	0.80	0.6
R_f (Ω)	18.8	0.9
Q_{dl} - Y_o (F s^{n-1})	6.7×10^{-7}	9.3
Q_{dl} - n	0.90	0.8
R_{ct} (Ω)	103	0.7

(B) MnOx-Pi catalyst

Parameters	Value	Error (%)
R_s (Ω)	2.5	4.1
Q_f - Y_o (F s^{n-1})	0.0002	3.0
Q_f - n	0.80	0.6
R_f (Ω)	18.4	1.1
Q_{dl} - Y_o (F s^{n-1})	8.7×10^{-7}	10
Q_{dl} - n	0.90	1.0
R_{ct} (Ω)	137	0.8

Furthermore, the Mott-Schottky plots at 1 kHz for MnOx-Pi and MnOx-Pi-rGO are compared in Fig. 11(b). According to Mott-Schottky equation,[58]

$$1 / C^2 = [2 / (\varepsilon_r \varepsilon_0 e N_d)] [E - E_{fb} - (k_B T / e)] \qquad (2)$$

where C is the capacitance of the space charge layer, e is the electronic charge, ε_r is the dielectric constant of the electrode material, ε_0 is the permittivity of air, N_d is the carrier density, E is the applied potential and E_{fb} is the flat band potential. Thus, the Mott-Schottky plot ($1/C^2$ vs. E) provides the flat band potential and charge carrier density. The flat band potential (Fig. 11(b)) for MnOx-Pi is 0.74 V whereas that of MnOx-Pi-rGO is 0.79 V. Both of them show positive slope which is typical for an n-type semiconductor. However, MnOx-Pi electrode shows slightly higher slope in comparison with MnOx-Pi-rGO. Since, the charge carrier (electrons for n-type semiconductor) density is inversely related to the slope of the Mott-Schottky plot, it is concluded that the carrier density is larger for MnOx-Pi-rGO catalyst compared to MnOx-Pi. Similarly, MnOx-Pi-rGO exhibited a smaller sheet resistance value in comparison with that of MnOx-Pi under identical deposition conditions (ESI, S5)

4. CONCLUSIONS

A Mn based composite catalyst, MnOx-Pi-rGO was prepared from a suspension of GO in neutral phosphate buffer solution consisting of $KMnO_4$. The manganese oxide incorporated phosphate ions and deposited on rGO sheets, which in turn was formed on the substrate electrode by electrochemical reduction of GO in the suspension. By varying the ratio of $KMnO_4$ and GO in the deposition medium and performing linear sweep voltammetry for OER, the optimum composition of the deposition medium was obtained as 20 mM $KMnO_4$ + 6.5 % GO in 0.1 M phosphate buffer electrolyte of pH 7. Under identical conditions, the MnOx-Pi-rGO catalyst exhibited 6.2 mA cm^{-2} OER current against 2.9 $mAcm^{-2}$ by MnOx-Pi catalyst at 2.05 V in neutral phosphate solution. The Tafel slopes measured for OER at MnOx-Pi and MnOx-Pi-rGO were similar in magnitude at about 0.180 V $decade^{-1}$. The high Tafel slopes were attributed to partial dissolution of the catalyst during oxygen evolution. The positive influence of rGO on catalytic activity of MnOx-Pi towards OER is demonstrated.

REFERENCES

[1]. E. Fabbri, A. Habereder, K. Waltar, R. Kotz and T. J. Schmidt, Developments and Perspectives of Oxide-based Catalysts for the Oxygen Evolution Reaction, *Catal. Sci. Technol.*, 2014, 4, 3800 - 3821.

[2]. C. C. L. McCrory, S. Jung, J. C. Peters and T. F. Jaramillo, Benchmarking Heterogeneous Electrocatalysts for the Oxygen Evolution Reaction, *J. Am. Chem. Soc.,* 2013, 135, 16977 - 16987.

[3]. Y. Lee, J. Suntivich, K. J. May, E. E. Perry and Y. Shao-Horn, Synthesis and Activities of Rutile IrO_2 and RuO_2 Nanoparticles for Oxygen Evolution in Acid and Alkaline Solutions, *J. Phys. Chem. Lett.,* 2012, 3, 399 - 404.

[4]. H. Over, Surface Chemistry of Ruthenium Dioxide in Heterogeneous Catalysis and Electrocatalysis: From Fundamental to Applied Research. *Chem. Rev.,* 2012, 112, 3356 - 3426.

[5]. M. E. G. Lyons and M. P. Brandon, The Oxygen Evolution Reaction on Passive Oxide Covered Transition Metal Electrodes in Alkaline Solution. Part III – Iron, *Int. J. Electrochem. Sci.,* 2008, 3, 1463 - 1503.

[6]. M. E. G. Lyons and M. P. Brandon, Redox Switching and Oxygen Evolution Electrocatalysis in Polymeric Iron Oxyhydroxide Films, *Phys. Chem. Chem. Phys.,* 2011, 13, 2203 - 2217.

[7]. J. A. Koza, Z. He, A. S. Miller and J. A. Switzer, Electrodeposition of Crystalline Co_3O_4 - A Catalyst for the Oxygen Evolution Reaction, *Chem. Mater.,* 2012, 24, 3567 - 3573.

[8]. X. Liu, J. Jiang and L. Ai, Non-precious Cobalt Oxalate Microstructures as Highly Efficient Electrocatalysts for Oxygen Evolution Reaction, *J. Mater. Chem. A,* 2015, 3, 9707 - 9713.

[9]. L. A. Stern and X. Hu, Enhanced Oxygen Evolution Activity by NiO_x and $Ni(OH)_2$ Nanoparticles, *Faraday Discuss.,* 2014, 176, 363 - 379.

[10]. Y. Qiu, L. Xin, and W. Li, Electrocatalytic Oxygen Evolution Over Supported Small Amorphous Ni–Fe Nanoparticles in Alkaline Electrolyte, *Langmuir,* 2014, 30, 7893 - 7901.

[11]. T. Kishi and K. Shiota, The Oxygen Evolution Reaction on Cobalt-containing β-MnO_2, *Surf. Coat. Tech.*, 1988, 3, 287 - 293.

[12]. M. Morita, C. Iwakura and H. Tamura, The Anodic Characteristics of Modified Mn Oxide Electrode: Ti/RuO_x/MnO_x, *Electrochim. Acta,* 1977, 23, 331 - 335.

[13]. Y. Gorlin and T. F. Jaramillo, A Bifunctional Nonprecious Metal Catalyst for Oxygen Reduction and Water Oxidation*, J. Am. Chem. Soc.,* 2010, 132, 13612 - 13614.

[14]. A. Ramirez, P. Hillebrand, D. Stellmach, M. M. May, P. Bogdanoff and S. Fiechter, Evaluation of MnO_x, Mn_2O_3 and Mn_3O_4 Electrodeposited Films for the Oxygen Evolution Reaction of Water, *J. Phys. Chem. C,* 2014, 118, 14073 - 14081.

[15]. C. X. Guo , S. Chen and X. Lu, Ethylenediamine-mediated Synthesis of Mn_3O_4 Nano-Octahedrons and their Performance as Electrocatalysts for the Oxygen Evolution Reaction, *Nanoscale,* 2014, 6, 10896 - 10901.

[16]. Z. Li, S. Shi, Q. Zhong, C. Zhang and C. Xu, Pt-Mn_3O_4/C as Efficient Electrocatalyst for Oxygen Evolution Reaction in Water Electrolysis, *Electrochim. Acta*, 2014, 146, 119 - 124.

[17]. R. N. Singh, J. P. Singh, H. N. Cong and P. Chartier, Effect of Partial Substitution of Cr on Electrocatalytic Properties of $MnFe_2O_4$ towards O_2 Evolution in Alkaline Medium, *Int. J. Hydrogen Energ,* 2006, 31, 1372 - 1378.

[18]. T. Pandiarajan, S. Ravichandran and L. J. Berchmans, Enhancing the Electro Catalytic Activity of Manganese Ferrite through Cerium Substitution for Oxygen Evolution in KOH Solution, *RSC Adv.,* 2014, 4, 64364 - 64370.

[19]. A. M. Mohammad, M. I. Awad and M. S. El-Deab, T. Okajima and T. Ohsaka, Electrocatalysis by Nanoparticles: Optimization of the Loading Level and Operating pH for the Oxygen Evolution at Crystallographically Oriented Manganese Oxide Nanorods Modified Electrodes, *Electrochim. Acta,* 2008, 53, 4351 - 4358.

[20]. M. Morita, C. Iwakura and H. Tamura, The Anodic Characteristics of Manganese Dioxide Electrodes Prepared by Thermal Decomposition of Manganese Nitrate, *Electrochim. Acta,* 1977, 22, 325 - 328.

[21]. M. S. El-Deab, M. I. Awad, A. M. Mohammad and T. Ohsaka, Enhanced Water Electrolysis: Electrocatalytic Generation of Oxygen Gas at Manganese Oxide Nanorods Modified Electrodes, *Electrochem. Commun.,* 2007, 9, 2082 - 2087.

[22]. M. Morita, C. Iwakura and H. Tamura, The Anodic Characteristics of Massive Manganese Oxide Electrode, *Electrochim. Acta,* 1979, 24, 357 - 362.

[23]. T. Takashima, K. Hashimoto and R. Nakamura, Mechanisms of pH-Dependent Activity for Water Oxidation to Molecular Oxygen by MnO_2 Electrocatalysts, *J. Am. Chem. Soc.,* 2012, 134, 1519 - 1527.

[24]. M. Huynh, D. K. Bediako and D. G. Nocera, Functionally Stable Manganese Oxide Oxygen Evolution Catalyst in Acid, *J. Am. Chem. Soc*., 2014, 136, 6002 - 6010.

[25]. I. Zaharieva, P. Chernev, M. Risch, K. Klingan, M. Kohlhoff, A. Fischer and H. Dau, Electrosynthesis, Functional, and Structural Characterization of a Water-Oxidizing Manganese Oxide, *Energy Environ. Sci.,* 2012, 5, 7081 - 7089.

[26]. D. Ye, T. Wu, H. Cao, Y. Wang, B. Liu, S. Zhang and J. Kong, Electrocatalysis of both Oxygen Reduction and Water Oxidation Using a Cost-Effective Three-Dimensional MnO_2/Graphene/Carbon nanotube, *RSC Adv.,* 2015, 5, 26710 - 26715.

[27]. W. Yuan, P. K. Shen and S. P. Jiang, Controllable Synthesis of Graphene Supported MnO_2 Nanowires via Self-Assembly for Enhanced Water Oxidation in Both Alkaline and Neutral Solutions, *J. Mater. Chem. A,* 2014, 2, 123 - 129.

[28]. J. Wei, Y. Liu, Y. Ding, C. Luo, X. Du and J. Lin, MnO_2 Spontaneously Coated on Carbon Nanotubes for Enhanced Water Oxidation, *Chem. Commun.,* 2014, 50, 11938 - 11941.

[29]. N. I. Andersen, A. Serov and P. Atanassov, Metal oxides/CNT Nano-Composite Catalysts for Oxygen Reduction/Oxygen Evolution in Alkaline Media, *Appl. Catal. B. Environmental,* 2015, 163, 623 - 627.

[30]. Z. Fan, J. Yan, T. Wei, L. Zhi, G. Ning, T. Li1 and F. Wei, Asymmetric Supercapacitors Based on Graphene/MnO_2 and Activated Carbon Nanofiber Electrodes with High Power and Energy Density, *Adv. Funct. Mate.,* 2011, 21, 2366 - 2375.

[31]. X. Huang, X. Qi, F. Boey and H. Zhang, Graphene-Based Composites, *Chem. Soc. Rev.,* 2012, 41, 666 - 686.

[32]. A. K. Geim and K. S. Novoselov, The Rise of Graphene, *Nat. Mater.,* 2007, 6, 183 - 191.

[33]. M. W. Kanan and D. G. Nocera, In Situ Formation of an Oxygen-Evolving Catalyst in Neutral Water Containing Phosphate and Co^{2+}, *Science,* 2008**,** 321, 1072 - 1075.

[34]. Y. Liu and D. G. Nocera, Spectroscopic Studies of Nanoparticulate Thin Films of a Cobalt-Based Oxygen Evolution Catalyst, *J. Phys. Chem. C,* 2014, 118, 17060 - 17066.

[35]. S. Hassan, M. Suzuki and A. A. El-Moneim, Facile Synthesis of MnO_2/graphene Electrode by Two-steps Electrodeposition for Energy Storage Application, *Int. J. Electrochem. Sci.,* 2014, 9, 8340 - 8354.

[36] J. N. Broughton and M. J. Brett, Variations in MnO_2 Electrodeposition for Electrochemical Capacitors, *Electrochim. Acta,* 2005, 50, 4814 - 4819.

[37] H. L. Guo, X. F. Wang, Q. Y. Qian, F. B. Wang and X. H. Xia, A Green Approach to the Synthesis of Graphene Nanosheets*, ACS Nano,* 2009, 3, 2653 - 2659.

[38] S. Y. Toh, K. S. Loh, S. K. Kamarudin and W. R. W. Daud, Graphene Production via Electrochemical Reduction of Graphene Oxide: Synthesis and Characterization, *Chem. Eng. J,* 2014, 251, 422 - 434.

[39]. W. S. Hummers and R. E. Offeman, Preparation of Graphitic Oxide, *J. Am. Chem. Soc.,* 1958, 80, 1339 - 1339.

[40]. I. Zhitomirsky, M. Cheong and J. Wei, The Cathodic Electrodeposition of Manganese Oxide Films for Electrochemical Supercapacitors, *JOM*, 2007, 59, 66 - 69.

[41]. Y. Zhan, M. Lu, S. Yang, C. Xu, Z. Liu and J. M. Lee, Activity of Transition-Metal (Manganese, Iron, Cobalt, and Nickel) Phosphates for Oxygen Electrocatalysis in Alkaline Solution. *Chem. Cat. Chem.,* 2016, 8, 372 - 379.

[42]. Y. Surendranath, M. Dinca and D. G. Nocera, Electrolyte-Dependent Electrosynthesis and Activity of Cobalt-Based Water Oxidation Catalysts, *J. Am. Chem. Soc.,* 2009, 131, 2615 - 2620.

[43]. Y. Surendranath, M. W. Kanan and D. G. Nocera, Mechanistic Studies of the Oxygen Evolution Reaction by a Cobalt-Phosphate Catalyst at Neutral pH, *J. Am. Chem. Soc.,* 2010, 132, 16501 - 16509.

[44]. D. Shevchenko, M. F. Anderlund, S. Styring, H. Dau, I. Zaharieva and A. Thapper, Water Oxidation by Manganese Oxides formed from Tetranuclear Precursor Complexes: The Influence of Phosphate on Structure and Activity, *Phys. Chem. Chem. Phys*., 2014, 16, 11965 - 11975.

[45]. M. Huynh, D. K. Bediako, Y. Liu, and D. G. Nocera, Nucleation and Growth Mechanisms of an Electrodeposited Manganese Oxide Oxygen Evolution Catalyst, *J. Phys. Chem. C,* 2014, 118, 17142 - 17152.

[46]. J. Yang and S. Gunasekaran, Electrochemically Reduced Graphene Oxide Sheets for Use in High Performance Supercapacitors, *Carbon,* 2013, 51, 36 - 44.

[47]. W. Li, C. Tan, M. A. Lowe, H. D. Abruna and D. C. Ralph, Electrochemistry of Individual Monolayer Graphene Sheets, *ACS Nano*, 2011, 5, 2264 - 2270.

[48] C. M. Fernandez-Posada, H. Amorin, C. Correas, O. Pena, M. Alguero and A. Castro, Mechanosynthesis and Multiferroic Properties of the $BiFeO_3$–$BiMnO_3$–$PbTiO_3$ Ternary System along its Morphotropic Phase Boundary, *J. Mater. Chem. C,* 2015, 3, 2255 - 2265.

[49]. A. Irshad and N. Munichandraiah, High Catalytic Activity of Amorphous Ir-Pi for Oxygen Evolution Reaction, *ACS Appl. Mater. Interfaces,* 2015, 7, 15765 - 15776.

[50]. S. Zhu, H. Zhang, P. Chen, L. H. Nie, C.H. Li and S. K. Li, Self-assembled Three-Dimensional Hierarchical Graphene Hybrid Hydrogels with Ultrathin β-MnO_2 Nanobelts for High Performance Supercapacitors, *J. Mater. Chem. A,* 2015, 3, 1540 - 1548.

[51]. M. A. Pimenta, G. Dresselhaus, M. S. Dresselhaus, L. G. Cancado, A. Jorioa and R. Saito, Studying Disorder in Graphite based Systems by Raman Spectroscopy, *Phys. Chem. Chem. Phys.,* 2007, 9, 1276 - 1291.

[52]. K. N. Kudin, B. Ozbas, H. C. Schniepp, R. K. Prudhomme, I. A. Aksay and R.Car, Raman Spectra of Graphite Oxide and Functionalized Graphene Sheets, *Nano Lett.,* 2008, 8, 36 - 41.

[53]. S. Y. Toh, K. S. Loh, S. K. Kamarudin and W. R. W. Daud, Graphene Production via Electrochemical Reduction of Graphene Oxide: Synthesis and Characterization, *Chem. Eng. J,* 2014, 251, 422 - 434.

[54]. G. Park, L. Bartolome, K. G. Lee, S. J. Lee, D. H. Kim and T. J. Park, One-Step Sonochemical Synthesis of a Graphene Oxide–Manganese Oxide Nanocomposite for Catalytic Glycolysis of Poly(ethylene terephthalate), *Nanoscale,* 2012, 4, 3879 - 3885.

[55]. K. Jin, J. Park, J. Lee, K. D. Yang, G. K. Pradhan, U. Sim, D. Jeong, H. L. Jang, S. Park, D. Kim, N. Sung, S. H. Kim, S. Han and K. T. Nam, Hydrated Manganese(II) Phosphate ($Mn_3(PO_4)_2 \cdot 3\ H_2O$) as a Water Oxidation Catalyst, *J. Am. Chem. Soc.,* 2014, 136, 7435 - 7443.

[56]. A. Irshad and N. Munichandraiah, An Oxygen Evolution Co-Ac Catalyst-the Synergistic Effect of Phosphate ions*, Phys. Chem. Chem. Phys.,* 2014, 16, 5412 - 5422.

[57]. J. O'M. Bokris and T. Otagawa, Mechanism of Oxygen Evolution on Perovskites, *J. Phys. Chem.,* 1983, 87, 2960 - 2971.

[58]. A. Irshad and N. Munichandraiah, Photochemical Deposition of Co-Ac Catalyst on ZnO Nanorods for Solar Water Oxidation, *J. Electrochem. Soc.,* 2015, 162, H235 - H243.

Figures and Captions

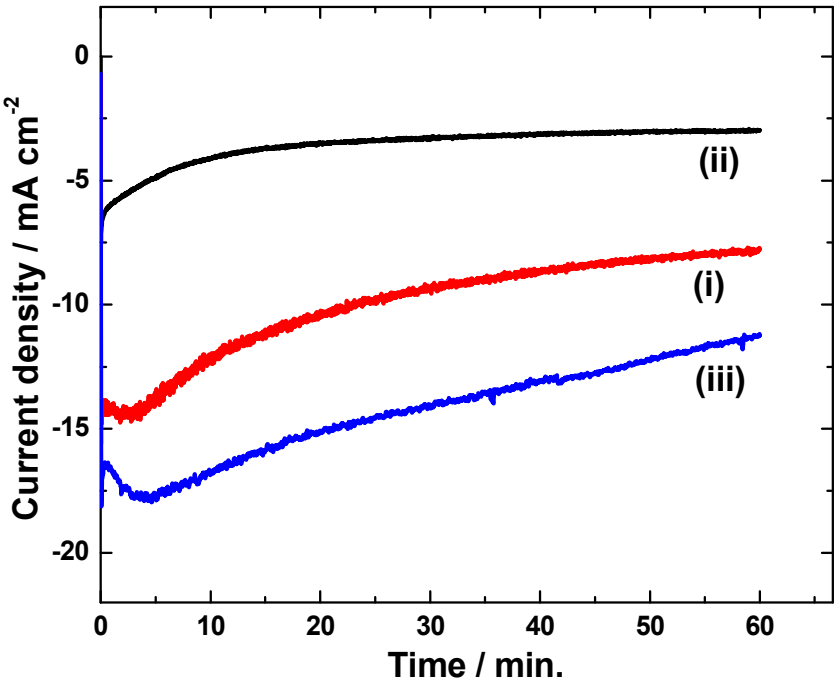

Fig. 1: Current density versus time plot during deposition at -1.05 V vs. SCE from 0.1 M phosphate solutions (pH 7.0) containing (i) 20 mM $KMnO_4$, (ii) GO and (iii) 20 mM $KMnO_4$ + GO. Concentration of GO was adjusted to 0.2 mg ml^{-1}.

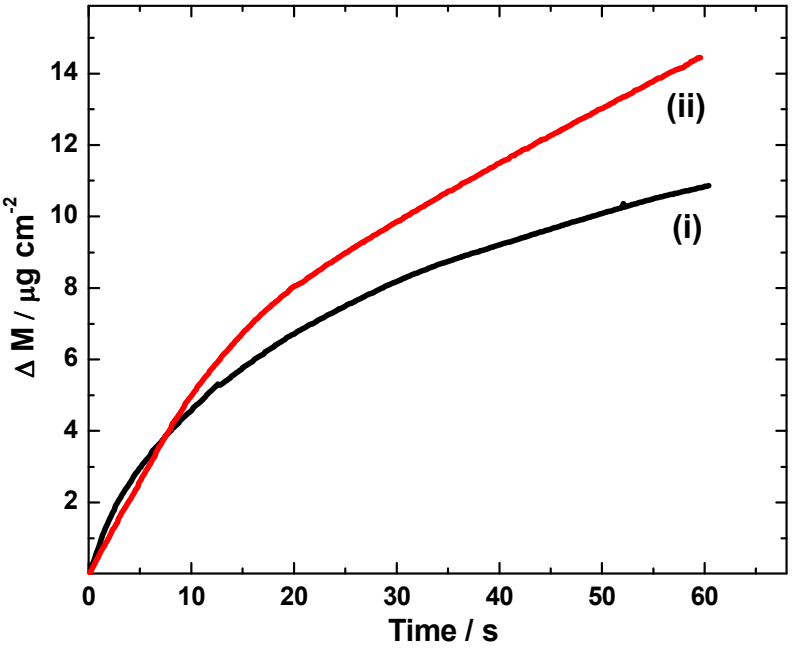

Fig. 2: Variation in mass during deposition at -1.05 V vs. SCE from 0.1 M phosphate solutions (pH 7.0) containing (i) 20 mM $KMnO_4$ and (iii) 20 mM $KMnO_4$ + 0.2 mg ml^{-1} GO.

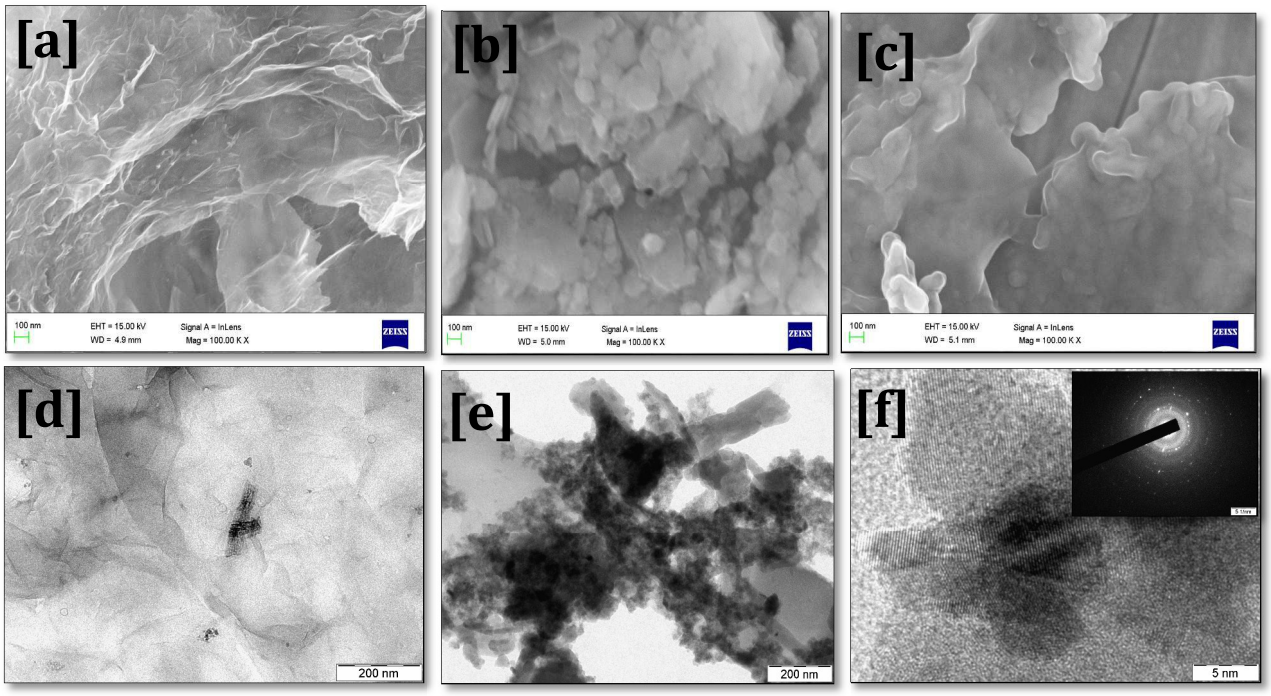

Fig 3: SEM micrographs for (a) rGO, (b) MnOx-Pi and (c) MnOx-Pi-rGO. TEM images for (d) rGO and (e, f) MnOx-Pi-rGO. Inset in (f) shows the SAED pattern for MnOx-Pi-rGO.

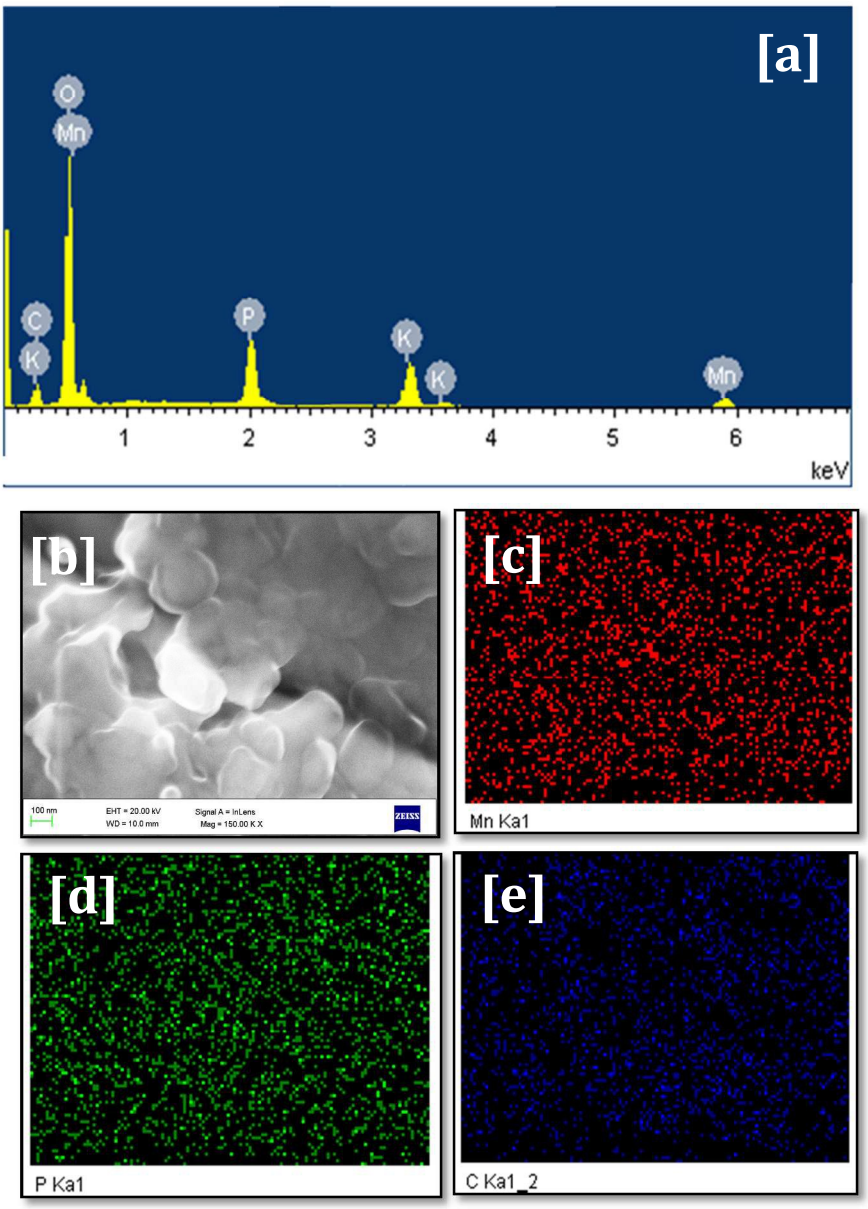

Fig. 4: (a). EDXA spectra and (b) SEM image of MnOx-Pi-rGO on Pt. X-ray maps showing the distribution of (c) Mn, (d) P and (e) C.

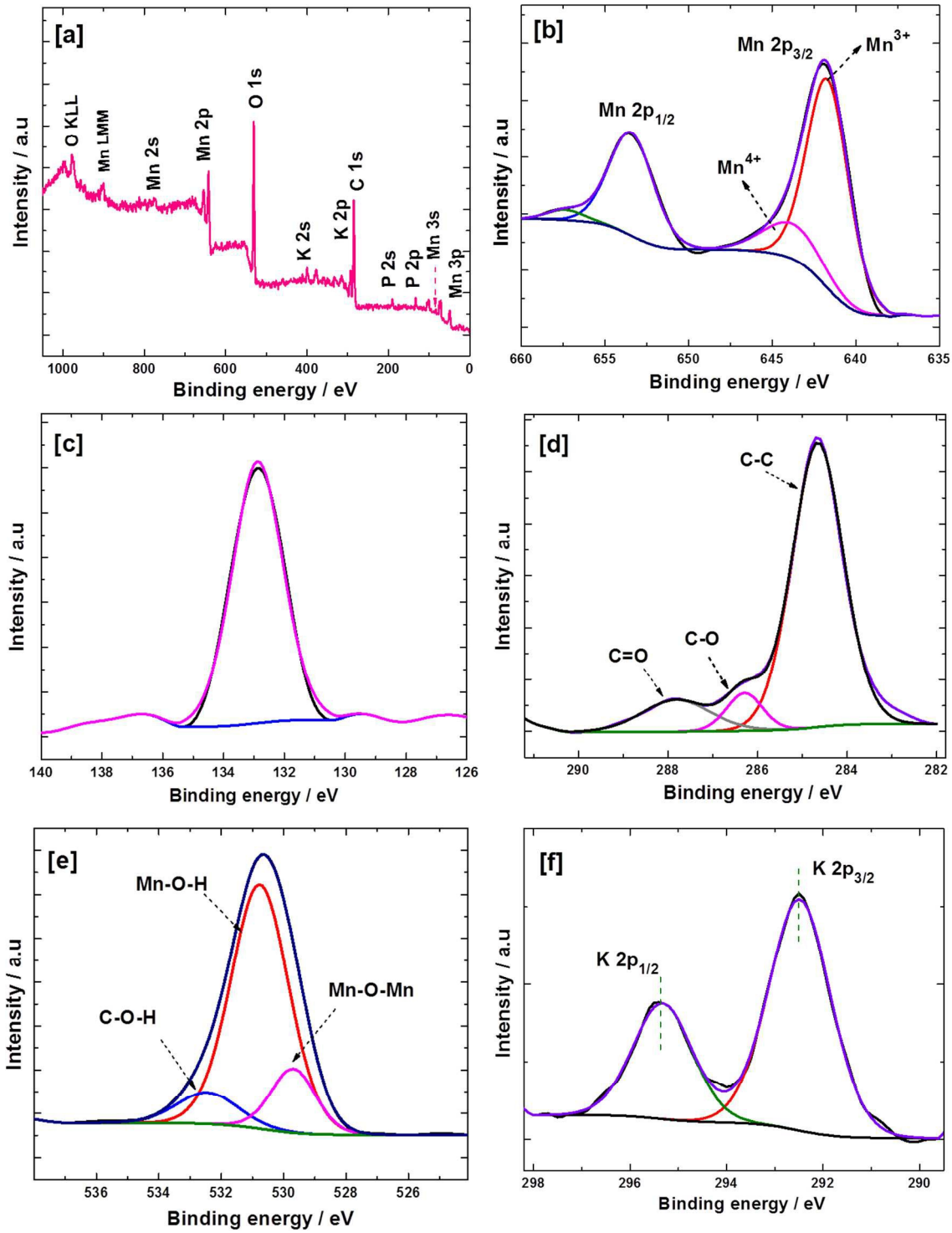

Fig. 5: XPS spectra for MnOx-Pi-rGO. (a) survey spectrum, and high resolution spectra for (b) Mn 2p, (c) P 2p, (d) C 1s, (e) O 1s and (f) K 2p.

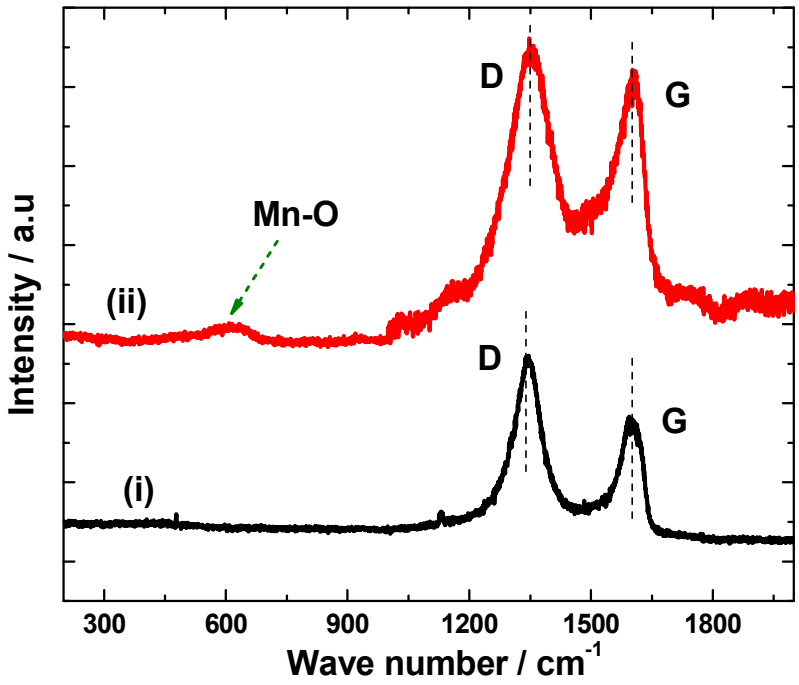

Fig. 6: Raman spectra for (i) rGO and (ii) MnOx-Pi-rGO. Excitation wave length: 532 nm.

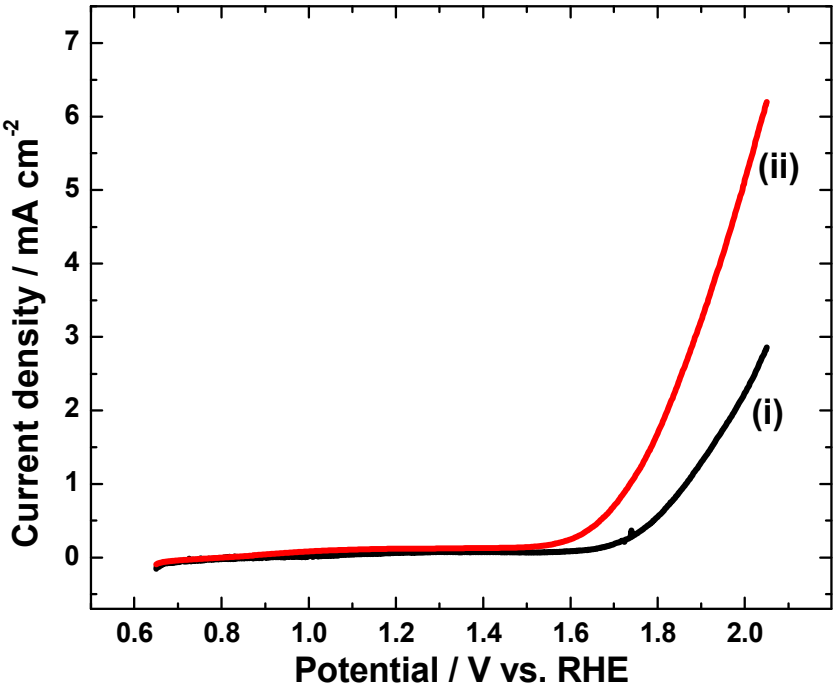

Fig. 7: Linear sweep voltammograms at 5 mV s^{-1} in 0.1 M neutral phosphate buffer solution using (i) MnOx-Pi and (ii) MnOx-Pi-rGO electrodes.

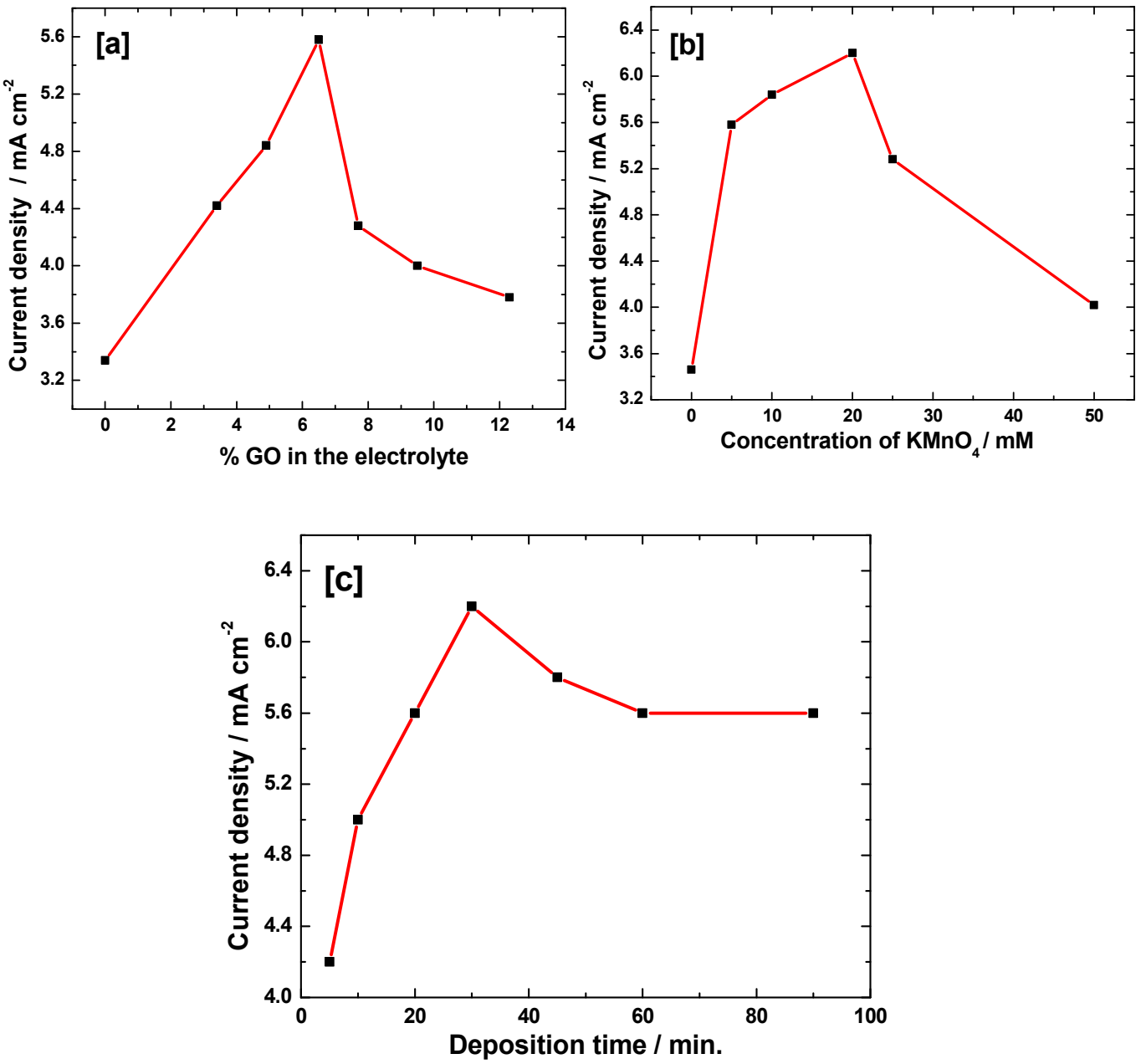

Fig. 8: (a).Current density at 2.05 V obtained for the electrodes deposited from 15 mM $KMnO_4$ + 0.1 M phosphate as the function of weight percentage of GO in the electrolyte. Similar plots for the electrodes (b) deposited from 6.5 % GO + 0.1 M phosphate solutions (pH 7.0) at different concentrations of $KMnO_4$ and (c) deposited from 20 mM $KMnO_4$ + 6.5 % GO + 0.1 M phosphate solutions (pH 7.0) for different time intervals.

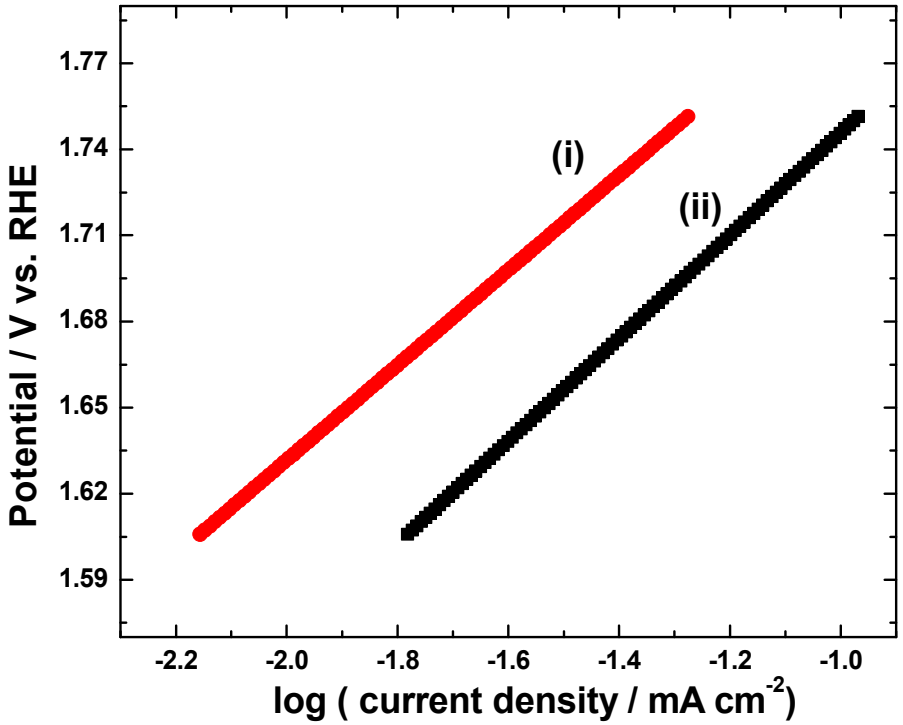

Fig. 9: Tafel plots for (i) MnOx-Pi and (ii) MnOx-Pi-rGO in 0.1 M neutral phosphate solution.

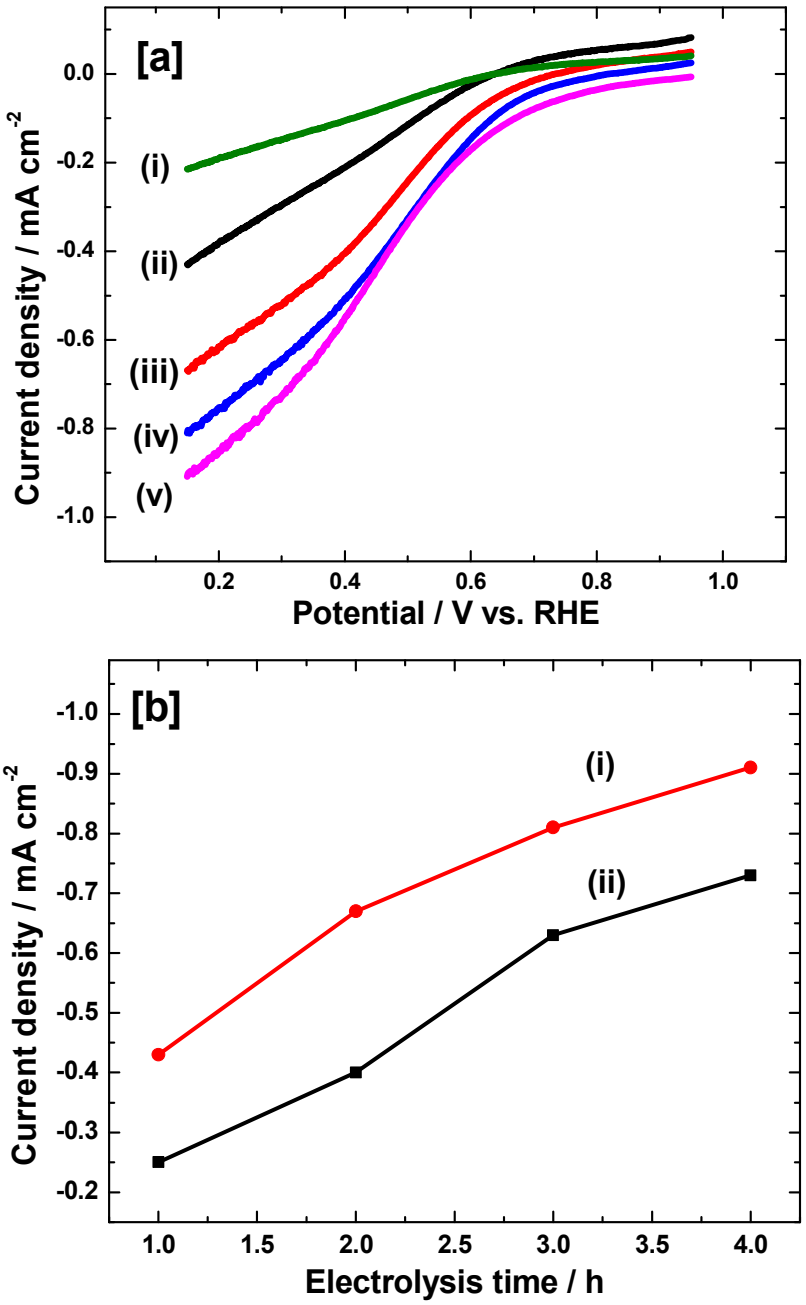

Fig. 10: (a) Linear sweep voltammetry for ORR on a Pt RDE after oxygen evolution reaction on a MnOx-Pi/C electrode at 2.05 V for (i) 1, (ii) 2, (iii) 3 and (iv) 4 h. Scan rate: 10 mV s^{-1} and rotation speed: 2500 rpm. (b) Variation in the ORR current density at 0.10 V versus electrolysis time for (i) MnOx-Pi-rGO and (ii) MnOx-Pi.

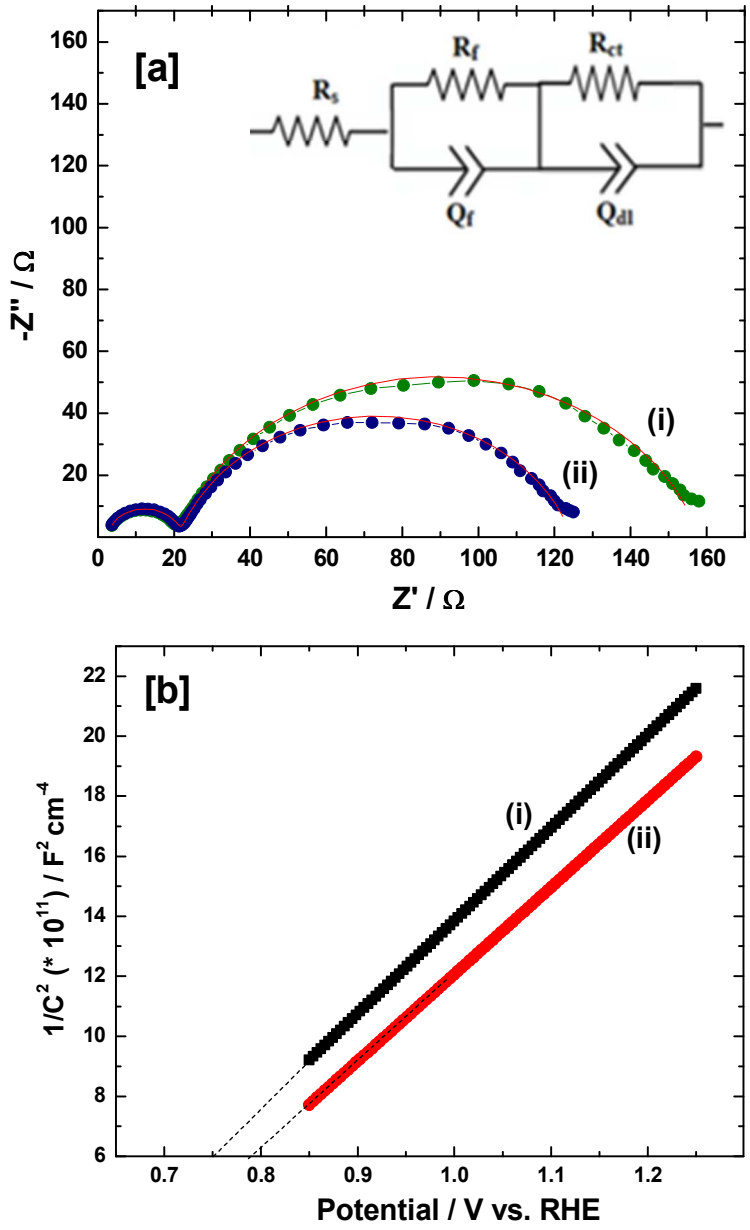

Fig. 11: (a) Nyquist plots at 1.95 V and (b) Mott-Schottky plot at 1 kHz for (i) MnOx-Pi and (ii) MnOx-Pi-rGO electrode in 0.1 M neutral phosphate solution.

Graphical Abstract

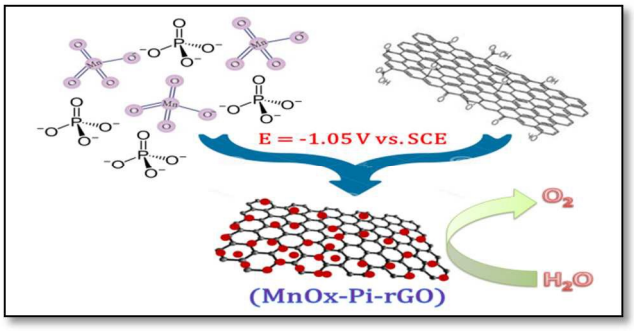

MnO_x-Pi-rGO OER catalyst is prepared by the simultaneous electrochemical reduction of MnO_4^- ions and GO in neutral phosphate electrolyte.